Physica D 51 (1991) 482–497
North-Holland

Fundamental interactions of vortical structures with boundary layers in two-dimensional flows

E.A. Coutsias[1] and J.P. Lynov

Association EURATOM–Risø National Laboratory, Optics and Fluid Dynamics Department, Risø National Laboratory, P.O. Box 49, DK-4000 Roskilde, Denmark

The effect of no-slip walls on the evolution of coherent, vortical structures in two-dimensional flows is studied by numerical calculations. The calculations are based on an accurate and efficient spectral scheme which has been developed for the solution of the 2D Navier–Stokes equations in the vorticity–stream function representation for bounded geometries. Fundamental processes connected to vorticity detachment from the boundary layers caused by the proximity of vortical structures are described. These processes include enstrophy enhancement of the main flow during bursting events, and pinning down of vortex dipoles by "vortex shielding".

1. Introduction

A basic property of many two-dimensional flow systems is the ability to support the existence of isolated coherent vortical structures for times which are very long compared to the turnaround time of the structures themselves. These vortical structures can be formed in a variety of ways, either by external forcing or by nonlinear amalgamation processes in freely decaying turbulence. Spectacular examples of such coherent vortices can be observed in the atmospheres of Jupiter and Neptune, but coherent vortices also play an important role in the large-scale fluid motions of the earth's atmosphere and oceans.

Many different laboratory experiments have demonstrated generation of essentially two-dimensional vortical structures. In ordinary fluids, the first stages of the evolution of perturbed shear layers [1] are predominantly two-dimensional processes under which coherent vortices form and coalesce. Experiments in rotating tanks [2–6], in stratified fluids [7], in soap-films [8], and in mercury subject to an external magnetic field [9, 10] also show the generation of various types of two-dimensional vortical structures, such as monopoles, dipoles and tripoles. In magnetically confined plasmas, Q-machine experiments [11–13] have demonstrated the generation and interaction of two-dimensional coherent structures, or convective cells, caused by cross-field electrostatic perturbations. These convective cells greatly enhance the cross-field plasma transport, a property which can be responsible for many of the problems with plasma confinement in large magnetic fusion experiments.

A number of numerical simulations have been performed to study various aspects of coherent vortices in two-dimensional flows. These studies include investigations of the emergence of isolated vortices in turbulent flows [14–19] and in perturbed shear layers [20–22], properties of isolated vortices [23, 24], and interactions between various vortical structures [25–33].

In this paper, the effect of no-slip walls on the evolution of vortical structures in two-dimensions

[1] Permanent address: Department of Mathematics and Statistics, University of New Mexico, Albuquerque, NM 87131, USA.

0167-2789/91/$03.50

is investigated by using an accurate and efficient spectral scheme [32] based on Chebyshev–Fourier expansions. It should be stressed that it is not the intention in the present paper to study the complex problem of transition [34] from laminar to turbulent flow at a no-slip boundary. For a transition, three-dimensional effects probably play an important role [35], so only fairly low resolution numerical studies can be carried out at present. In this work, it will be assumed that the two-dimensional vortical structures are created by some mechanism at a distance from the walls. This makes it easier to separate the development of the boundary layer from the generation process of the coherent vortices. Specifically, two different processes are investigated. The first is the effect of no-slip walls on the roll-up of a perturbed shear layer, and the second is the collision of a vortex dipole with no-slip wall. In both cases, vorticity detachments from the boundary layer are observed to occur in sudden bursting events. In the latter case, it is found that the motion of the impinging dipole is stopped by shielding of the two vortices in the original dipole by rings of boundary layer vorticity.

The paper is organized as follows. Section 2 describes some properties of the basic equations. In particular, the problem connected to the overdeterminacy of the Poisson equation for the stream function due to the no-slip boundaries is addressed. This problem is resolved analytically by expanding the fields in Fourier–Chebyshev series and imposing necessary and sufficient integral solvability constraints on the vorticity field. In section 3 the numerical scheme is briefly discussed, and section 4 contains a description of the results. Finally, some concluding remarks are included in section 5.

2. Basic equations

The basic equations describing the two-dimensional flows under investigation are the Navier–Stokes (N–S) equations, which consist of the momentum equation

$$\frac{\partial \boldsymbol{u}}{\partial t} + \boldsymbol{u} \cdot \nabla \boldsymbol{u} = -\nabla p + \nu \nabla^2 \boldsymbol{u} \tag{1}$$

and the continuity equation

$$\nabla \cdot \boldsymbol{u} = 0. \tag{2}$$

Here, $\boldsymbol{u}$ is the flow velocity, p the pressure, and ν the kinematic viscosity.

The flows considered in this paper are assumed to take place in a channel which is periodic in the x direction with periodicity length L and bounded in the y direction by no-slip walls at $y = \pm 1$. The x and y variables are normalized by a characteristic length scale L_0. If furthermore a characteristic velocity, U_0, is introduced, all variables in eqs. (1), (2) can be made dimensionless by proper combinations of L_0 and U_0. The normalized viscosity ν obtained in this manner is the reciprocal of the Reynolds number

$$\mathrm{Re} \equiv \frac{U_0 L_0}{\nu_\mathrm{f}}, \tag{3}$$

where ν_f is the fluid viscosity in physical dimensions.

Eqs. (1), (2) express the N–S equations in the "primitive variable" or the "velocity–pressure" (V–P) formulation. Taking the curl of (1) leads to

$$\frac{\partial \omega}{\partial t} + J(\omega, \psi) = \nu \nabla^2 \omega, \tag{4}$$

where the scalar vorticity ω is given by

$$\boldsymbol{\omega} = \omega \hat{\boldsymbol{z}}, \tag{5}$$

the stream function ψ by

$$u = \nabla\psi \times \hat{z}, \tag{6}$$

and the Jacobian $J(f, g)$ is defined as

$$J(f, g) \equiv \frac{\partial f}{\partial x}\frac{\partial g}{\partial y} - \frac{\partial g}{\partial x}\frac{\partial f}{\partial y}. \tag{7}$$

By taking the curl of (6) it is seen that the stream function ψ satisfies the Poisson equation

$$\nabla^2\psi = \omega. \tag{8}$$

Eqs. (4) and (8) give the N–S equations in the "vorticity–stream function" (V–S) formulation, which will be employed in the following. In this formulation, the incompressibility condition (2) is automatically satisfied.

2.1. Boundary conditions

The fields are now Fourier expanded in the x direction according to

$$\begin{pmatrix} \omega(x, y) \\ \psi(x, y) \end{pmatrix} \sim \sum_{n=-N/2}^{N/2-1} \begin{pmatrix} \omega_n(y) \\ \psi_n(y) \end{pmatrix} \exp\left(\mathrm{i}\frac{2\pi}{L}nx\right), \tag{9}$$

where the subindex n now indicates a field in Fourier (or mode) space.

Introducing the no-slip boundary conditions

$$u(x, y = \pm 1) = U^{\pm}\hat{x} \tag{10}$$

the stream function is found to satisfy the Neumann boundary conditions

$$\left.\frac{\partial\psi_0}{\partial y}\right|_{y=\pm 1} = U^{\pm},$$

$$\left.\frac{\partial\psi_n}{\partial y}\right|_{y=\pm 1} = 0, \quad n \neq 0, \tag{11}$$

as well as the Dirichlet boundary conditions

$$\psi_0(\pm 1) = F^{\pm}(t),$$

$$\psi_n(\pm 1) = 0, \quad n \neq 0, \tag{12}$$

where $F^{\pm}(t)$ are arbitrary functions of time.

These boundary conditions (11), (12) will cause the Poisson equation (8) to be overdetermined unless some constraints are imposed on $\omega_n(y)$. In the following discussion of how these "solvability constraints" [33] are determined, the two cases $n \neq 0$ and $n = 0$ are investigated separately.

2.1.1. Fourier mode $n \neq 0$

Inserting the Fourier expansions (9) into Poisson's equation (8) gives

$$\frac{\mathrm{d}^2\psi_n}{\mathrm{d}y^2} - \lambda_n^2\psi_n = \omega_n, \tag{13}$$

where

$$\lambda_n \equiv \frac{2\pi n}{L}. \tag{14}$$

In (13), the y derivative has been written as an ordinary derivative. This is done in order to simplify the following discussion and is justified by the lack of explicit time dependence in the Poisson equation (8).

Eq. (13) is subject to both the Dirichlet boundary conditions

$$\psi_n(\pm 1) = 0, \tag{15}$$

the stream function ψ by

$$u = \nabla\psi \times \hat{z}, \tag{6}$$

and the Jacobian $J(f, g)$ is defined as

$$J(f, g) \equiv \frac{\partial f}{\partial x}\frac{\partial g}{\partial y} - \frac{\partial g}{\partial x}\frac{\partial f}{\partial y}. \tag{7}$$

By taking the curl of (6) it is seen that the stream function ψ satisfies the Poisson equation

$$\nabla^2\psi = \omega. \tag{8}$$

Eqs. (4) and (8) give the N–S equations in the "vorticity–stream function" (V–S) formulation, which will be employed in the following. In this formulation, the incompressibility condition (2) is automatically satisfied.

2.1. Boundary conditions

The fields are now Fourier expanded in the x direction according to

$$\begin{pmatrix} \omega(x, y) \\ \psi(x, y) \end{pmatrix} \sim \sum_{n=-N/2}^{N/2-1} \begin{pmatrix} \omega_n(y) \\ \psi_n(y) \end{pmatrix} \exp\left(\mathrm{i}\frac{2\pi}{L}nx\right), \tag{9}$$

where the subindex n now indicates a field in Fourier (or mode) space.

Introducing the no-slip boundary conditions

$$u(x, y = \pm 1) = U^{\pm}\hat{x} \tag{10}$$

the stream function is found to satisfy the Neumann boundary conditions

$$\left.\frac{\partial\psi_0}{\partial y}\right|_{y=\pm 1} = U^{\pm},$$

$$\left.\frac{\partial\psi_n}{\partial y}\right|_{y=\pm 1} = 0, \quad n \neq 0, \tag{11}$$

as well as the Dirichlet boundary conditions

$$\psi_0(\pm 1) = F^{\pm}(t),$$

$$\psi_n(\pm 1) = 0, \quad n \neq 0, \tag{12}$$

where $F^{\pm}(t)$ are arbitrary functions of time.

These boundary conditions (11), (12) will cause the Poisson equation (8) to be overdetermined unless some constraints are imposed on $\omega_n(y)$. In the following discussion of how these "solvability constraints" [33] are determined, the two cases $n \neq 0$ and $n = 0$ are investigated separately.

2.1.1. Fourier mode $n \neq 0$

Inserting the Fourier expansions (9) into Poisson's equation (8) gives

$$\frac{\mathrm{d}^2\psi_n}{\mathrm{d}y^2} - \lambda_n^2\psi_n = \omega_n, \tag{13}$$

where

$$\lambda_n \equiv \frac{2\pi n}{L}. \tag{14}$$

In (13), the y derivative has been written as an ordinary derivative. This is done in order to simplify the following discussion and is justified by the lack of explicit time dependence in the Poisson equation (8).

Eq. (13) is subject to both the Dirichlet boundary conditions

$$\psi_n(\pm 1) = 0, \tag{15}$$

to

$$B_{mn}^{\pm} = \sum_{p=0}^{P-1} (\pm 1)^{p-1} p^2 \sigma_{mnp}. \tag{28}$$

Thus, for each Fourier mode n different from 0, a Poisson–Dirichlet problem (20), (21) must be solved for each forcing Chebyshev mode $T_m(y)$. In order to resolve the sharp boundary layers in the fields $\sigma_{mn}(y)$ for high values of n, it has been found that the number of Chebyshev modes, P, used in the expansion (27) of $\sigma_{mn}(y)$ must exceed the number of Chebyshev forcing modes by approximately 40. Since (20) only depends on n^2, the values of $B_{mn}^{\pm}$ are the same for cosine and sine terms.

It should be emphasized that the determination of $B_{mn}^{\pm}$ is independent of the value of ν and only needs to be performed once for each different geometry, i.e. it depends only on L besides M and N. Values of $B_{mn}^{\pm}$ obtained for high values of M and/or N can directly be used in lower resolution runs. These properties are in contrast to the characteristics of the scheme by Dennis and Quartapelle [36] for determination of no-slip boundary constraints. Their scheme also makes use of the velocity–stream function formulation, but requires an additional Poisson equation to be solved per Fourier mode at each time step. Thus, although the present scheme requires $\mathcal{O}(M \times N)$ Poisson equations to be solved, this calculation is performed once and for all (for each different geometry), which is much faster than the Dennis–Quartapelle scheme for typical simulations of dynamical flow processes.

2.1.2. Fourier mode $n = 0$

In this case the no-slip conditions are

$$\left.\frac{\partial \psi_0}{\partial y}\right|_{y=\pm 1} = U^{\pm}, \quad \psi_0(y = \pm 1) = F^{\pm}(t). \tag{29}$$

The value $\psi_0(y)$ contains an arbitrary constant, since only $\partial\psi_0/\partial y$ enters the N–S equations. There is consequently freedom to choose one of the functions $F^+(t)$ or $F^-(t)$, while the other remains unknown.

In order to preserve the velocity difference between the flow at the two walls, the vorticity must maintain the circulation, C, where

$$C \equiv \oint_{\partial D} u \cdot \mathrm{d}l = L(U^- - U^+)$$

$$= \int_D \omega \, \mathrm{d}s = L \int_{-1}^{+1} \omega_0(y, t) \, \mathrm{d}y. \tag{30}$$

Here, D and ∂D are the surface and boundary of the two-dimensional flow, respectively.

Given $\omega(y, t = 0)$, the Galilean invariance of the N–S equations allows both U^+ and U^- to be determined by choosing a frame of reference. In the following, the choice $U^- = -U^+$ is made.

The temporal evolution of C can be found by surface integration of (4), which yields

$$\frac{\mathrm{d}C}{\mathrm{d}t} = \nu L \left(\left.\frac{\partial \omega_0}{\partial y}\right|_{y=+1} - \left.\frac{\partial \omega_0}{\partial y}\right|_{y=-1} \right). \tag{31}$$

The requirement that $\mathrm{d}C/\mathrm{d}t = 0$ subsequently imposes the constraint

$$\left.\frac{\partial \omega_0}{\partial y}\right|_{y=+1} - \left.\frac{\partial \omega_0}{\partial y}\right|_{y=-1} = 0. \tag{32}$$

It is seen that conservation of C either requires enforcement of

$$\int_{-1}^{+1} \omega_0(y, t) \, \mathrm{d}y = \int_{-1}^{+1} \omega_0(y, 0) \, \mathrm{d}y \tag{33}$$

or eq. (32), which only amounts to one constraint on $\omega_0(y)$. A second constraint can be found by

integrating the x component of the moment equation in primitive variables (1) along the walls at $y = \pm 1$, which gives

$$\left.\frac{\partial \omega_0}{\partial y}\right|_{y=\pm 1} = -\frac{1}{L\nu}\,\delta p|_{y=\pm 1}, \tag{34}$$

where $\delta p|_{y=\pm 1}$ is the total pressure difference along a length of period of the channel at either wall. The two conditions in (34) are consistent with (32) provided that

$$\delta p|_{y=+1} = \delta p|_{y=-1} = \delta p. \tag{35}$$

Thus, for $n = 0$ eqs. (32), (34) and (35) give the two constraints

$$\left.\frac{\partial \omega_0}{\partial y}\right|_{y=+1} = \left.\frac{\partial \omega_0}{\partial y}\right|_{y=-1} = -\frac{1}{L\nu}\,\delta p. \tag{36}$$

Provided a perfect numerical time integration these constraints ensure the conservation of circulation C. Consequently, a time history of $C(t)$ can serve as a measure of accuracy of the numerical code.

For the Poisson equation with $n = 0$, the Neumann conditions $(\partial\psi_0/\partial y)|_{y=\pm 1} = U^{\pm}$ are employed with

$$U^- = -U^+ = \frac{1}{2}\int_{-1}^{+1} \omega_0(y, t=0)\,\mathrm{d}y. \tag{37}$$

Since $\psi_n(y)$ is expanded in Chebyshev polynomials as written in (23), the coefficient ψ_{0n} is left undetermined by (37). The freedom to add any constant value to $\psi_0(y)$, as discussed above, is then used to set

$$\psi_{00} = 0. \tag{38}$$

2.2. Initial vorticity distribution

The code is initialized by choosing a vorticity distribution at $t = 0$. This initial vorticity distribution must, naturally, satisfy the no-slip boundary conditions (10). If the coefficients $\omega_{mn}(t=0)$ from (23) and $B^{\pm}_{mn}$ from (28) are considered as the components of an M-dimensional vector for fixed $n \neq 0$, then the initial guess for $\tilde{\omega}_{mn}(t=0)$ has to be projected normally onto a plane containing the vectors with the components B^+_{mn} and B^-_{mn}. Since the vectors with the components B^+_{mn} and B^-_{mn} are generally not mutually orthogonal, two vectors with the components

$$b^{\mathrm{e}}_{mn} = \tfrac{1}{2}(B^+_{mn} + B^-_{mn}), \quad b^{\mathrm{o}}_{mn} = \tfrac{1}{2}(B^+_{mn} - B^-_{mn}) \tag{39}$$

are introduced. It is clear from (28) that these two vectors are orthogonal to each other.

The projection of the initial guess for $\tilde{\omega}_{mn}(t=0)$ onto the true no-slip $\omega_{mn}(t=0)$ is then performed by

$$\omega_{mn} = \tilde{\omega}_{mn} - \frac{\tilde{\omega}_{mn}\cdot b^{\mathrm{e}}_{mn}}{\|b^{\mathrm{e}}_{mn}\|^2} b^{\mathrm{e}}_{mn} - \frac{\tilde{\omega}_{mn}\cdot b^{\mathrm{o}}_{mn}}{\|b^{\mathrm{o}}_{mn}\|^2} b^{\mathrm{o}}_{mn}. \tag{40}$$

In order for this projection scheme to give reasonable results, the initial guess $\tilde{\omega}_{mn}$ should not be too far from satisfying the no-slip constraints (25). This can typically be achieved by choosing a zero-order distribution which gives rise to a flow parallel to the walls and adding an arbitrary, but not too large perturbation.

2.3. Energy and enstrophy evolution

The temporal evolution of the total energy, $E \equiv \frac{1}{2}\int_{\mathrm{D}} |\boldsymbol{u}|^2\,\mathrm{d}s$, and the total enstrophy, $\Omega \equiv \int_{\mathrm{D}} \omega^2\,\mathrm{d}s$, can be found from (1) and (4). The

results are

$$\frac{\mathrm{d}E}{\mathrm{d}t} = -\nu\Omega + \nu L(U^-\omega^- - U^+\omega^+) - \delta p \int_{-1}^{+1} \frac{\partial \psi_0}{\partial y}\,\mathrm{d}y \tag{41}$$

and

$$\frac{\mathrm{d}\Omega}{\mathrm{d}t} = \nu \int_{\partial \mathrm{D}} (\nabla\omega^2)\cdot \boldsymbol{n}\,\mathrm{d}l - 2\nu \int_{\mathrm{D}} (\nabla\omega)^2\,\mathrm{d}s, \tag{42}$$

where $\boldsymbol{n}$ is the outgoing normal to the boundary. It is seen that the terms originating from surface integrations over D are all negative. The only way for energy or enstrophy to increase in the flow is via the boundary terms calculated along ∂D. Eqs. (41) and (42) will be used as accuracy checks of the numerical code.

3. Numerical scheme

Insertion of the Fourier–Chebyshev expansions described by (9) and (23) into Poisson's equation (8) yields

$$\sum_{\substack{p=m+2 \\ p+m \text{ even}}}^{M} p(p^2 - m^2)\psi_{pn} - \lambda_n^2 \psi_{mn} = -\omega_{mn}, \tag{43}$$

where λ_n is given by (14). The Dirichlet boundary conditions (15) for $n \neq 0$ give

$$\sum_{m=0}^{M} (\pm 1)^m \psi_{mn} = 0, \quad \text{for } n \neq 0, \tag{44}$$

while the Neumann boundary conditions from (29) together with (38) result in

$$\sum_{m=1}^{M} (\pm 1)^{m-1} m^2 \psi_{m0} = U^{\pm}, \quad \psi_{00} = 0, \tag{45}$$

where $U^{\pm}$ is defined by (37).

Following the "tau-method" [37, 38], the last two rows in (43) are replaced by either (44), if $n \neq 0$, or (45), if $n = 0$. The resulting system

$$A_{mp}\psi_{pn} = \tilde{\omega}_{mn}, \tag{46}$$

where $\tilde{\omega}_{mn} = \omega_{mn}$ except for $\tilde{\omega}_{(M-1)0} = U^+, \tilde{\omega}_{M0} = U^-$ and $\tilde{\omega}_{(M-1)n} = \tilde{\omega}_{Mn} = 0$, for $n = 1, \ldots, N$. The matrix $\mathbf{A}$ is regular and contains zeroes below the main diagonal (except for the last two rows). Direct solution of (46) requires $\mathcal{O}(M^3N)$ operations, which is unacceptable since $\psi(x, y)$ must be determined at every time step. However, Chebyshev recursion relations [37] allow the transformation of $\mathbf{A}$ into a tri-diagonal submatrix above the last two rows, which contain the boundary conditions. Subsequent Gauss elimination produces a lower triangular, tri-diagonal matrix ready for solution by direct forward substitution. These row operations are only performed initially on $\mathbf{A}$. The actual solution of Poisson's equation by this scheme requires only $\mathcal{O}(MN)$ operations. It has been proven [39] that such recursions can be derived for the second derivative operator for a wide class of orthogonal polynomial families obeying 3-term recursion relations of the type satisfied by symmetric Jacobi polynomials.

The Chebyshev–Fourier expansion of the vorticity dynamical equation (4) is straightforward. The nonlinear products in the convective term described by the Jacobian are computed in point space and the result fully dealiased using the $\frac{2}{3}$ truncation scheme [32, 37, 38].

For the time integration of (4), the presence of both a nonlinear convective term and a linear diffusion term necessitates the use of a mixed explicit–implicit scheme. A 3rd order Adams–Bashforth predictor–corrector scheme is used for the former term and a backwards Euler scheme for the latter. This means that at the kth step, a Helmholtz equation of the form

$$\left(I - \nu\delta t\, \Delta_N^M\right)\omega^{k+1} = F^k \tag{47}$$

has to be solved for both the predictor and the corrector step. In (47) δt is the time step, Δ_N^M is the finite approximation to the Laplacian operator by M Chebyshev and N Fourier modes, and F^k represents the terms which are already resolved by the explicit predictor and corrector steps. As in the case of the Poisson equation, the vorticity constraints enter via the tau-method, which, for each Fourier mode n, means replacing the last two rows in (47) corresponding to the two highest Chebyshev modes by either (25), for $n \neq 0$, or (36), for $n = 0$. The scheme for the numerical solution of the Helmholtz equation (47) is equivalent to the scheme discussed above for the solution of the Poisson equation. Due to the high efficiency of the Poisson and Helmholtz solvers, most of the time in the code is spent in the FFT routines, which are already very efficient.

4. Numerical results

This section contains results from three different runs. An account of the basic parameters for the runs of and the results obtained for the accuracy checks is given in table 1. The runs were performed on Risø's Apollo DN10000 "mini-supercomputer" and used approximately 60 CPU hours each.

In the first example, the effect of no-slip walls on the roll-up of a perturbed shear layer is investigated. The functional form of the initial vorticity distribution before projection is

$$\tilde{\omega}(x, y) = 6\left[\operatorname{sech}^2(5y) - \cos x\right]\left(1 - y^2\right)^4, \tag{48}$$

Table 1
Characteristic parameters for the simulations. The variables L, ν, M, N and δt designate the channel length, the viscosity, the number of Chebyshev modes, the number of Fourier modes and the time step, respectively. The values listed for the three different accuracy checks are all obtained at the final time step of each run. The "C check" measures the accuracy of circulation conservation by integration of the vorticity field. The value for this parameter is given relative for run 1, and absolute for runs 2 and 3. The values of "$\mathrm{d}E/\mathrm{d}t$ check" and "$\mathrm{d}\Omega/\mathrm{d}t$ check" are obtained by comparing the values obtained directly from code, based on time centered differences among three consecutive values of E and Ω, with the values obtained by evaluating (41) and (42). Both these accuracy checks express relative deviations.

	Run 1	Run 2	Run 3
Flow	roll-up	dipole, 90°	dipole, 80°
L	2π	4	4
ν	2×10^{-3}	10^{-3}	10^{-3}
M	256	256	256
N	256	512	512
δt	5×10^{-4}	2.5×10^{-4}	2.5×10^{-4}
Time steps	14000	7000	7000
C check	3×10^{-8}	4×10^{-15}	10^{-3}
$\mathrm{d}E/\mathrm{d}t$ check	2×10^{-3}	10^{-5}	10^{-5}
$\mathrm{d}\Omega/\mathrm{d}t$ check	10^{-5}	6×10^{-3}	3×10^{-2}

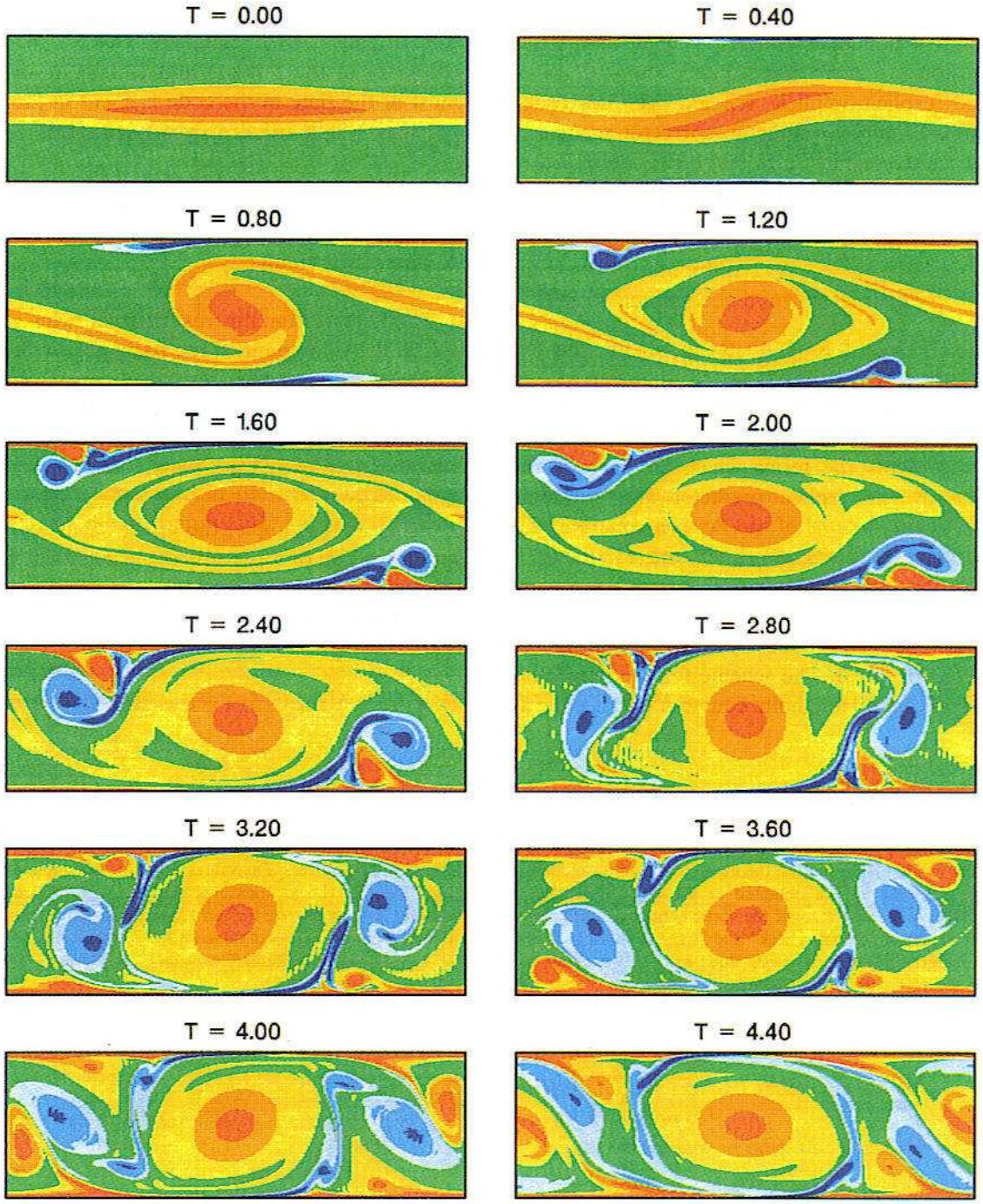

Fig. 1. Contour plots of the vorticity distribution, $\omega(x, y)$, at various times for the shear layer roll-up in run 1. Blue colors correspond to negative values, red/orange colors to positive values, and the green color corresponds to vorticity values centered around zero.

which is projected onto a distribution satisfying the no-slip boundary conditions by the scheme described in section 2.2. The effect of this projection is not noticeable on the contour plot of $\omega(x, y, t = 0)$.

Fig. 1 contains contour plots showing the temporal evolution of $\omega(x, y)$. Red and blue colors indicate regions of positive and negative vorticity, respectively. Fig. 2 shows the corresponding evolution of the normalized total energy, $E/E(0)$ (shown with a dashed line), and normalized total enstrophy, $\Omega/\Omega(0)$.

From fig. 1, it is seen that the initial stage of the roll-up process is fairly unaffected by the presence of the no-slip walls. However, as the positive vorticity, originally confined to the center of the channel, starts approaching the walls, regions of negative vorticity are generated in the boundary layers. Fig. 2 shows that the energy in the flow is continuously diminishing due to the effect of viscosity, but that the total enstrophy, Ω, is greatly increased over its initial value. As discussed in section 2.3, the values of E and Ω can only increase due to the behavior of the flow at the boundaries of the channel. The first bump on the trace of $\Omega(t)$ occurs at $t \sim 1.3$. At this time, part of the negative vorticity region in the boundary layer has slided over a region of positive vorticity nearer to the wall, and a formation of a dipolar structure is initiated. This dipolar structure has its propagation velocity directed into the main flow, and subsequently starts a detachment process from the wall. However, the strong shear in the main flow opposes this detachment and a complicated growth of dipole structure continues in the boundary layer.

The next hump in $\Omega(t)$ occurs at $t \sim 2.4$, when the dipolar structure in the boundary layer has gained enough strength to start entering the main flow. However, since the flow topology contains a saddle point near the location of the structure, the two parts of the dipolar structure are soon torn apart, and only the negative vorticity part continues into the central flow. The maximum peak in $\Omega(t)$ occurs at $t \sim 2.7$, which is about the time of this tearing event. After the splitting of the dipolar structure, the negative vorticity part is driven by the main flow to the other side of the channel. Here it quickly finds a positive counterpart, with whom it forms a new dipolar structure and enters the main flow again. The subsequent history of the evolution is rather chaotic, or turbulent, with dipolar structures continuously colliding with each other or torn apart by stresses in flow. At the same time new dipolar structures are being created in the boundary layers and give rise to sudden "bursting" increases of total enstrophy.

Although the flow in its later stages is turbulent, at any instant it still contains only relatively few vortical structures. However, contrary to the numerical results by McWilliams [14] for freely decaying two-dimensional turbulence in a doubly periodic domain, these vortical structures cannot be traced back to local extrema in the initial vorticity distribution. The origin of the structures in the present simulations are in the boundary layers, and the formation processes require the proximity of some other vortical structure in the main flow to the boundary layer. The generation of vortical structures in boundary layers caused by other vortical structures has been observed by Sommeria [9, 10] in experiments performed in mercury subject to an external magnetic field.

As a numerical artifact, low amplitude, wave-like structures in the x direction are seen to appear in $\omega(x, y)$ at $t \sim 2.4$. These waves are caused by numerical inaccuracies due to the finite number of Fourier modes N and are propagated in the simulations due to the dispersive character of the error of the 3rd order Adams–Bashforth scheme. These waves could be suppressed by either increasing the viscosity, but this would wash out the details of the flow, or by doubling N and using half the time step, but this would lead to more than a quadrupling of the total CPU time. In any case, the evolution of the flow would not change qualitatively, since the accuracy checks listed in table 1 are rather good, even for this run.

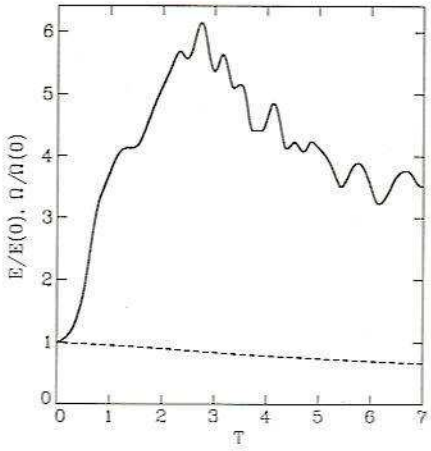

Fig. 2. Time evolution of the normalized total energy, $E(t)/E(0)$ (dashed line), and the normalized total enstrophy, $\Omega(t)/\Omega(0)$ (solid line), for the roll-up case shown in fig. 1.

It is clear from the results presented in figs. 1 and 2 that dipolar structures play an important role in the evolution of two-dimensional turbulence in a flow with no-slip walls. In order to investigate the behavior of such structures in more detail, some numerical calculations were performed on the interaction of isolated dipoles with no-slip walls. In these runs, the initial vorticity before projection is

$$\tilde{\omega}(x,y) = \frac{10\gamma_{11}}{R^2 J_0(\gamma_{11})} J_1\left(\frac{\gamma_{11} r}{R}\right) \times \left[(x-2)\cos\theta_0 + y\sin\theta_0\right], \quad \text{if } r \le R,$$
$$= 0, \quad \text{if } r > R, \tag{49}$$

where $r = \sqrt{\left[(x-2)^2 + y^2\right]}$, $R = 0.4$, $J_{0,1}(r)$ are the zero and first order Bessel functions, γ_{11} is the first zero of $J_1(r)$, and θ_0 is the initial injection angle. As in the first run, $\tilde{\omega}(x,y)$ is projected onto the no-slip $\omega(x,y)$ according to (40).

Figs. 3 and 4 are similar to figs. 1 and 2, but for the case of a dipole injected perpendicularly to a wall with $\theta_0 = 90°$. From the contour plots of $\omega(x,y)$, it is seen that the two parts of the origi-

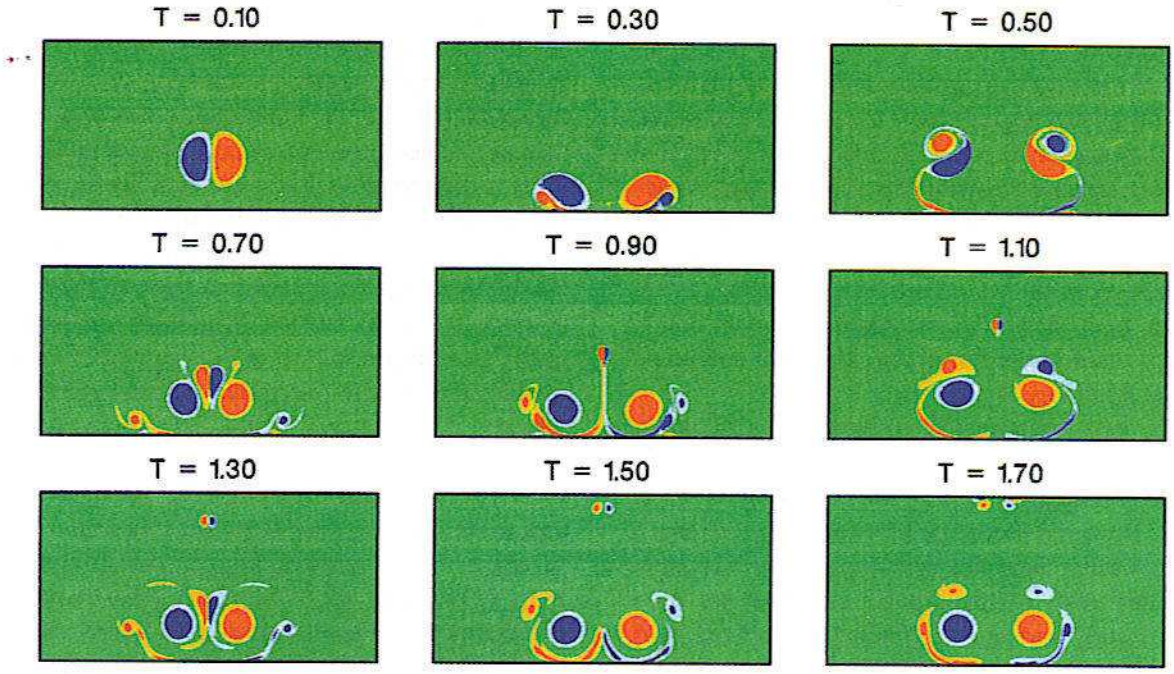

Fig. 3. Same as fig. 1 for the dipole–wall collision at 90° in run 2.

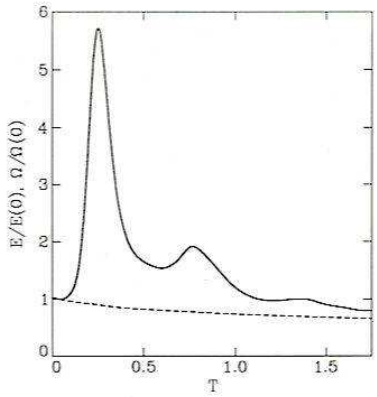

Fig. 4. Same as fig. 2 for the dipole–wall collision at 90° shown in fig. 3.

nal dipole split from each other when approaching the wall. If the walls were free-slip, the two parts would propagate away from each other along the walls under the influence of their mirror images. However, as seen in the previous example, a coherent vortical structure near a boundary layer at a no-slip wall generates a region of opposite vorticity. In fig. 4, it is seen that $\Omega(t)$ reaches a maximum at $t \sim 0.25$, which is the time of initial detachment of the newly created dipolar structures from the wall.

These new dipolar structures do not have balanced amounts of positive and negative vorticity and consequently they have curved trajectories. At $t \sim 0.6$, the two structures get close to each other, and, as a result of this encounter, the two dipolar structures exchange partners. Similar behaviour has also been seen in experiments [7, 8, 10] as well as in other numerical simulations [8, 25, 30].

After the splitting of the dipolar structures, one small dipole, consisting entirely of material originally close to the lower wall, propagates straight up, while a larger dipolar structure consisting of fluid from the original dipole starts a downward motion again. The second hump in $\Omega(t)$, at $t \sim 0.75$, corresponds to detachment of boundary layer vorticity at the second impact of dipolar structure at the lower wall. Although two new dipolar structures are formed out of incoming vortical structures and generated boundary layer vorticity, the second impact between these new dipolar structures out in the channel has a different outcome than the first collision. The second time there is no exchange of partners, and the boundary layer material is squeezed down again between the two major monopolar structures.

At $t \sim 1.5$, the small dipole has propagated all the way to the upper wall, and a mirror process of the original dipole collision with the lower wall is initiated, only at a smaller scale. After $t \sim 1.3$, the two parts of the original dipole seem to have become pinned down at a distance from the lower wall similar to their own diameters. If two monopoles of equal strength and opposite vorticity are isolated in an infinite fluid, they will move together with a joint velocity determined by the strength of their vorticity and their separation. The more or less complete stop of the two parts of the original dipole must be attributed to the (incomplete) ring of vorticity originating from the boundary layer and surrounding each monopolar structure. As a result of these vorticity rings or "halos", the two monopolar structures are in effect shielded from each other.

This behaviour is very similar to the results obtained by Shebalin [40] from simulations of vortex wake descent. It is known that an airplane moving through air generates two counter-rotating cylindrical vortices aligned along the direction of motion of the plane and with a vortex extending backwards from each wing tip. The directions of rotation for a lifting wing are such that the joint dipolar structure propagates downward. As the plane approaches a landing field, the dipolar, wing tip vortex system descends to the ground after the plane. It is also known that wing tip vortices can hover at some height over a landing field for long periods after a plane has landed. This is a behavior of great practical importance, since it imposes a lower limit to the admissible time separation between two landings.

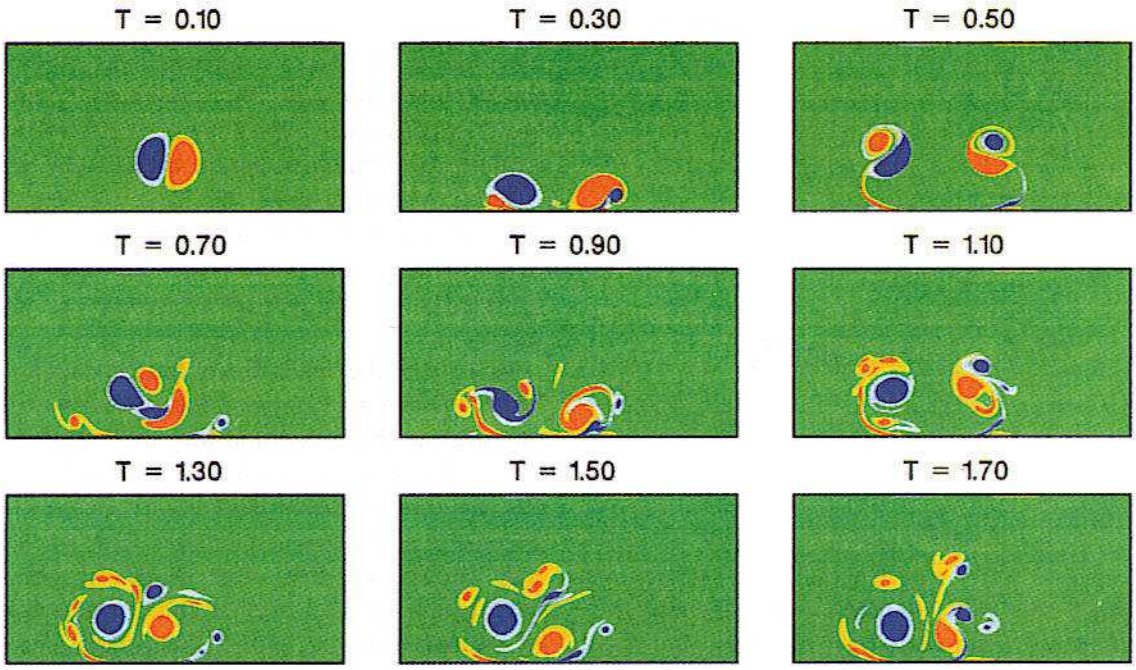

Fig. 5. Same as fig. 1 for the dipole–wall collision at 80° in run 3.

In the simulations of Shebalin, a rectangular two-dimensional domain with no-slip walls on two opposing sides was employed. The implementation of the no-slip boundary conditions was only approximate (as also stated by the author), and the resolution of the simulation was only 32×32 Fourier modes. Furthermore, the system of dynamical equations was slightly different from the ones used in the present paper, due to inclusion of temperature variation effects. Nevertheless, the temporal evolutions of the total enstrophy in Shebalin's simulations are qualitatively very similar to the plot of $\Omega(t)$ in fig. 4. Furthermore, the wing tip vortices in his simulations settle down near a constant height above the lower boundary in connection with a process that resembles the ring-like shielding discussed above, although the details seen in fig. 3 are absent in his low resolution runs.

In order to test the stability of the shielding process against changes in injection angle θ_0, a run was performed with $\theta_0 = 80°$, but otherwise with the same parameters as in run 2. The results

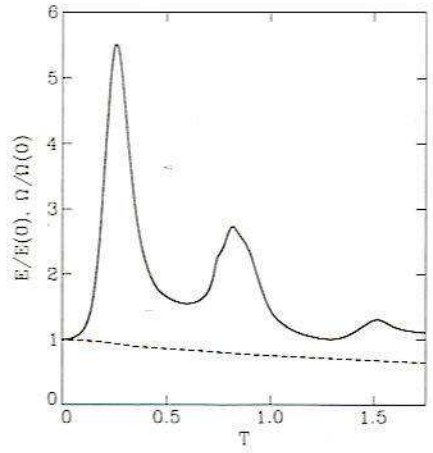

Fig. 6. Same as fig. 2 for the dipole–wall collision at 80° shown in fig. 5.

are shown in figs. 5 and 6, with the graphical representations used above. The evolution of the flow up to $t \sim 0.6$ is very similar to the case for run 2. However, after this time, which corresponds to the first collision between the two dipolar structures, the evolution is quite different.

Due to the oblique injection angle, the collision is not symmetric, and no exchange of partners occurs. In spite of the very different details of the flow evolution after the first dipole collision, the evolutions of total energy and enstrophy are qualitatively equivalent for the two runs. Also, in run 3 a new small dipolar structure, consisting of boundary layer material and capable of escaping into the upper part of the channel, is formed. This dipolar structure can be seen on the contour plot of $\omega(x, y, t = 1.7)$ in fig. 5. However, contrary to the case in run 2, this structure will not propagate along a straight path due to the imbalance of negative and positive vorticity.

5. Conclusion

In this paper, some fundamental interactions of vortical structures with boundary layers in two-dimensional flows have been investigated by numerical simulations. An approximation method in terms of Chebyshev–Fourier expansions of the problem of no-slip boundary conditions for the Navier–Stokes equations in the vorticity–stream function formulation was described. The method of enforcing the no-slip boundary conditions via tau constraints appears to be new. It was discussed how this solution can be implemented effectively in a numerical scheme.

The numerical code was used to simulate the evolution of three different flows in a periodic channel with no-slip walls. The first example was a roll-up of a perturbed shear layer, initially confined to the central part of the channel, while the two other examples showed the collision with no-slip walls of dipoles injected at 90° and 80° to the wall, respectively.

The roll-up process showed strong enhancement of the total enstrophy of the flow in sudden "bursting" events. These events were connected to the detachment of vorticity from the boundary layers in the form of dipolar structures. The detachments were caused by the proximity of vortical structures in the main flow to the boundary layers. Although the development of the flow became rather chaotic, only relatively few coherent structures were present in the flow at any instant. An interesting and open question is whether decaying, two-dimensional turbulent flows in a domain bounded by no-slip walls will approach one of the equilibrium states of minimum dissipation, which are known from studies [41, 42] of two-dimensional flows without these boundary conditions.

The interaction of a dipole injected perpendicularly onto a no-slip wall was also found to generate vortical structures of opposite polarity in the boundary layer. The generated vortical structures formed two new dipolar structures together with the original vortical structures in the impinging dipole. These new dipolar structures detached from the boundary layer, thereby enhancing the enstrophy, and entered back into the channel. A subsequent collision between these new dipolar structures created yet a new, but smaller, dipolar structure, this time entirely consisting of boundary layer material. This small dipole progated straight across the channel, initiating a new collision process on the other side. The original dipole got pinned down by an effect called "shielding". This effect was caused by boundary layer vorticity continuously being pulled in a ring or "halo" around the two monopolar structures of the original dipole. The relevance of this effect to the practical problem of wing tip vortex pairs descending from landing aircrafts and hovering for long times over landing fields was discussed.

Finally, the role of injection angle on the interaction between a dipole and the boundary layer was investigated by changing the angle to 80°. Although details of the flow were very different between the two dipole runs, similar qualitative evolution of energy and enstrophy was observed.

It should be mentioned that the effects of extending these flow simulations to three dimensions are not known and need further investigation.

Acknowledgements

The helpful assistance of Bjarne Wallin in operating the computer at Risø is gratefully acknowledged. The authors have also benefited from enlightening discussions with D. Montgomery and J.V. Shebalin.

Note added in proof

Prof. G.J.F. van Heijst has brought to our attention the experimental work on dipole collisions against solid walls by van Heijst and Flor, in: Mesoscale/Synoptic Coherent Structures in Geophysical Turbulence, eds. J.C.J. Nihoul and B.M. Jamart (Elsevier, Amsterdam, 1989) pp. 591–608. Prof. van Heijst also communicated a manuscript by P. Orlandi on numerical simulations of vortex dipoles impinging on flat boundaries. This manuscript has recently been published (P. Orlandi, Phys. Fluids A 2 (1990) 1429–1436). The results reported in both these papers are in close agreement with the results reported here.

References

[1] C.M. Ho and P. Huerre, Ann. Rev. Fluid Mech. 16 (1984) 365.
[2] E.J. Hopfinger, F.K. Browand and Y. Gagne, J. Fluid Mech. 125 (1982) 505.
[3] S.V. Antipov, M.V. Nezlin, V.K. Rodionov, A.Yu. Rylov, E.N. Snezhkin, A.S. Trubnikov and A.V. Khutoretskii, Sov. J. Plasma Phys. 14 (1988) 648.
[4] G.J.F. van Heijst, J. Fluid Mech. 206 (1989) 171.
[5] G.J.F. van Heijst, P.A. Davies and R.G. Davis, Phys. Fluids A 2 (1990) 150.
[6] G.J.F. van Heijst and R.C. Kloosterziel, Nature 338 (1989) 569.
[7] G.J.F. van Heijst and J.B. Flór, Nature 340 (1989) 212.
[8] Y. Couder and C. Basdevant, J. Fluid Mech. 173 (1986) 225.
[9] J. Sommeria, J. Fluid Mech. 189 (1988) 553.
[10] J.-M. Nguyen Duc and J. Sommeria, J. Fluid Mech. 192 (1988) 175.
[11] H.L. Pécseli, J. Juul Rasmussen and K. Thomsen, Phys. Rev. Lett. 52 (1984) 2148.
[12] H.L. Pécseli, J. Juul Rasmussen and K. Thomsen, Plasma Phys. Contr. Fusion 27 (1985) 837.
[13] T. Huld, A.H. Nielsen, H.L. Pécseli and J. Juul Rasmussen, Phys. Rev. Lett. 64 (1990) 3023.
[14] J.C. McWilliams, J. Fluid Mech. 146 (1984) 21.
[15] A. Babiano, C. Basdevant, B. Legras and R. Sadourny, J. Fluid Mech. 183 (1987) 379.
[16] B. Legras, P. Santangelo and R. Benzi, Europhys. Lett. 5 (1988) 37.
[17] M.E. Brachet, M. Meneguzzi, H. Politano and P.L. Sulem, J. Fluid Mech. 194 (1988) 333.
[18] P.S. Marcus, Nature 334 (1988) 693.
[19] P. Santangelo, R. Benzi and B. Legras, Phys. Fluids A 1 (1989) 1027.
[20] G.M. Corcos and F.S. Sherman, J. Fluid Mech. 139 (1984) 29.
[21] D.G. Dritschel, J. Fluid Mech. 206 (1989) 193.
[22] G.P. Klaassen and W.R. Peltier, J. Fluid Mech. 202 (1989) 367.
[23] M.V. Melander, J.C. McWilliams and N.J. Zabusky, J. Fluid Mech. 178 (1987) 137.
[24] J.C. McWilliams, G.R. Flierl, V.D. Larichev and G.M. Reznik, Dyn. Atmos. Oceans (1981) 219.
[25] J.C. McWilliams and N.J. Zabusky, Geophys. Astrophys. Fluid Dyn. 19 (1982) 207.
[26] J.C. McWilliams, Geophys. Astrophys. Fluid Dyn. 24 (1983) 1.
[27] M.V. Melander, N.J. Zabusky and J.C. McWilliams, Phys. Fluids 30 (1987) 2612.
[28] M.V. Melander, N.J. Zabusky and J.C. McWilliams, J. Fluid Mech. 195 (1988) 303.
[29] E.A. Overman II and N.J. Zabusky, Phys. Fluids 25 (1982) 1297.
[30] M. Makino, T. Kamimura and T. Taniuti, J. Phys. Soc. Jpn. 50 (1981) 980.
[31] K. Tsuboi and Y. Oshima, J. Phys. Soc. Jpn. 54 (1985) 2137.
[32] E.A. Coutsias, F.R. Hansen, T. Huld, G. Knorr and J.P. Lynov, Phys. Scr. 40 (1989) 270.
[33] E.A. Coutsias, T. Huld and J.P. Lynov, in: Preprint Volume of the Ninth Symposium on Turbulence and Diffusion (American Meteorological Society, Boston, MA, 1990) p. 212.
[34] R. Betchov, in: Handbook of Turbulence, Vol. 1, eds. W. Frost and T.H. Moulden (Plenum, New York, 1977).
[35] S.A. Orszag and A.T. Patera, Phys. Rev. Lett. 45 (1980) 989.
[36] S.C.R. Dennis and L. Quartapelle, J. Comput. Phys. 52 (1983) 448.

[37] D. Gottlieb and S.A. Orszag, Numerical Analysis of Spectral Methods: Theory and Applications, SIAM CBMS-NSF Reg. Conf. Ser. in Appl. Math., Vol. 26 (SIAM, Philadelphia, 1977).
[38] C. Canuto, M.Y. Hussaini, A. Quarteroni and T.A. Zang, Spectral Methods in Fluid Dynamics, Springer Series in Computational Physics (Springer, Berlin, 1987).
[39] E.A. Coutsias, in preparation.
[40] J.V. Shebalin, preprint AIAA 87-0370 (1987).
[41] A.C. Ting, H.H. Chen and Y.C. Lee, Physica D 26 (1987) 37.
[42] D. Montgomery, in: Trends in Theoretical Physics, Vol. 1, eds. P.J. Ellis and Y.C. Tang (Addison–Wesley, New York, 1989) p. 239.